

Numerical simulation of bubble deformation and breakup under simple linear shear flows

Mitsuhiro Ohta^{a,b,*}, Tetsuya Ueta^b, Yozo Toei^c, Edwin Jimenez^d, Mark Sussman^e

^a organization=Department of Mechanical Science, Graduate School of Technology,
Industrial and Social Sciences, Tokushima University, addressline=2-1
Minamijyousanjima-cho, state=Tokushima 770-8506, country=Japan

^b organization=Department of Mechanical Engineering, Graduate School of Technology,
Industrial and Social Sciences, Tokushima University, addressline=2-1
Minamijyousanjima-cho, state=Tokushima 770-8506, country=Japan

^c organization=High Performance Plastics Company, Sekisui Chemical Co., Ltd.,
addressline=2-1 Hyakuyama, Mishimagun Shimamoto-cho, state=Osaka 618-0021,
country=Japan

^d organization=Spectral Numerical, LLC, addressline=1942 Broadway St., STE 314C,
city=Boulder, state=CO 80302, country=USA

^e organization=Department of Mathematics, Florida State University, city=Tallahassee,
state=FL 32306, country=USA

Abstract

Numerical simulations are presented for the deformation and breakup of a bubble in liquids undergoing simple linear shear flow. Numerical results are obtained using a hydrodynamic scheme with formal second-order accuracy based on a coupled level set/volume-of-fluid (CLSVOF) method. To verify our numerical algorithm and provide a basis for comparison, we also present simulation results that compare with previous, more popular, drop deformation and rupture simulations. The numerical results reveal that the shear-induced bubble deformation and breakup process differs significantly from that of the analogous drop system under similar flow conditions. The first distinguishing factor for bubble breakup is that the magnitude of shear flow necessary for causing rupture is much larger than that in the drop system case. In other words, a larger Reynolds number is needed to induce bubble breakup. The second distinct feature of the bubble system versus the drop system is that the bubble does not maintain a stable deformed shape as the system parameters approach

*Corresponding author: m-ohta@tokushima-u.ac.jp

the critical “breakup” Reynolds number. It is asserted that the differences in morphology for a bubble undergoing breakup versus a drop in the same process can be attributed to the density and viscosity ratio of the corresponding two-phase flow systems. The critical conditions for bubble breakup with respect to the Reynolds and capillary numbers are determined for several cases.

Keywords: Bubble deformation, bubble breakup, shear flow, CFD

1. Introduction

Bubble dynamics in shear flow, *including breakup*, is critically important for various scientific and engineering processes. We refer the reader to the following experimental studies relating to bubble deformation in foaming processes, microfluidic devices, and microbubbles in the blood circulation system,[4, 23, 3, 8]. In particular, it is the study of bubble deformation as it pertains to high-performance plastics applications that motivate this work. This article presents computational studies of shear-driven deformation *and breakup* of a bubble in insoluble viscous liquids. Studying bubble break-up via computation rather than experiments simplifies the process of setting a combination of precise, simple shear flow conditions, low Ca conditions, low-density ratio (1:1000), and low viscosity ratios (1:100). The physical properties that distinguish bubble and drop studies are expressed in terms of the density ratio $\lambda = \rho_b/\rho_m$ and the viscosity ratio $\eta = \mu_b/\mu_m$, where ρ is the fluid density, μ is the viscosity and the subscripts “b” and “m” denote the “bubble” or “drop” and the “matrix fluid”, respectively. For a bubble in an insoluble, viscous liquid, $\lambda \simeq 0$ and $\eta \simeq 0$, whereas most studies dealing with a drop in an immiscible viscous liquid take $\lambda = 1$ and $\eta \simeq 1$.

In this work, we focus on identifying critical flow states numerically, in terms of dimensionless quantities, that specify the extreme conditions at which a bubble in shear flow first transitions from deformation to breakup. We validate our numerical method by examining the sensitivity of the critical bubble deformation and break-up flow states with respect to the grid size. An advantage of

studying shear-driven bubble deformation and breakup computationally rather than experimentally is that we can easily modify fluid physical properties to ascertain the sensitivity of deformation and breakup to physical parameters. In our computations, the time-evolution of the boundary between gas and liquid is tracked with a coupled level set/volume-of-fluid (CLSVOF) interface capturing algorithm [36, 38]. We focus on determining critical physical conditions in which the breakup of a bubble occurs in shear flow because it is important to identify the parameter regimes in which a relatively simple system transitions from stable to unstable. Specifically, we ascertain the critical Reynolds number (Re_c) corresponding to the bubble breakup onset condition as a function of Ca .

In previous studies on the motion of bubble deformation in a simple shear flow [32, 23], only findings for bubble deformation under very low Re number conditions ($Re \ll 1$) have been reported. In this work, we determine, for the first time, the critical Reynolds number ($Re \gg 1$) that leads to *bubble* breakup. Additionally, our computational studies reveal characteristics that distinguish a drop's deformation and breakup processes versus those of a bubble.

We remark that there have been a number of articles on the study of lift of *slightly* deformable bubbles[9, 21]. We reiterate, though, that for bubble deformation *and breakup* in shear flows, only a few articles exist: [44, 43]. These previous studies mainly examined the dynamics (e.g., rotation angle) of bubble deformation in shear flow. Concerning bubble breakup, Wei et al. [44] presented only one numerical result for a bubble breakup process under the condition of Ca (Capillary number) = 35.

To highlight the mechanisms of bubble deformation and breakup in a shear flow, we juxtapose the bubble results with those of a drop. We remark that while the study of critical tensile strength parameters for the bubble is sparse, there have been many studies for the simpler drop problem. For completeness, we give a brief overview of previous “tensile strength” studies pertaining to drops.

The study of the deformation *and breakup* of a drop in immiscible viscous liquids undergoing simple linear shear flow has been investigated exten-

sively due to its fundamental importance to emulsion processes, materials processing, mixing, and reaction devices. The pioneering experimental work on this problem was performed by Taylor in the early 1930s [40, 41], and the subsequent theoretical and experimental progress up to the 1980s and 1990s was reviewed in [25] and [33], respectively. By the 2000s, progress in computational fluid dynamics (CFD) techniques and increased access to powerful computing resources led to a surge of research focused on direct simulations of this problem. In particular, detailed computational investigations of drop breakup, based on a Volume-of-Fluid (VOF) method [11] were presented in [22, 29, 31, 30, 18, 26, 27, 28]. Since then, the literature on computational studies on the deformation and breakup of a single or several drops in shear flow has continued to grow [6, 13, 45, 2, 15, 7, 19, 20, 14, 10, 1, 48] and a variety of numerical techniques have been developed to tackle this problem, including boundary-integral approaches [5, 16], lattice Boltzmann methods [12, 19], front tracking schemes [42], and interface-capturing level set methods [37].

2. Problem Description

Figure 1(a) shows a schematic of the computational system for our studies of a bubble (or drop) in shear flow. The computational domain consists of a three-dimensional rectangular domain of L (length) \times W (width) \times H (height). The size of L , W and H was determined after consideration of numerical result sensitivity to domain size; numerical studies of domain-size dependence are presented in Section 3.3. All computational results that follow were obtained from numerical solutions of the three-dimensional governing equations for gas-liquid/liquid-liquid flows. Computations are initialized with a spherical bubble (or drop) of radius $R = 5$ mm set at the center of the computational domain. The bubble (or drop) is then subjected to a linear shear flow generated by the motion of the top and bottom plates, which have constant velocity $+V$ and $-V$, respectively. In the interior of the domain, the initial velocity condition is assumed to be a simple linear profile and periodic boundary conditions are

84 imposed along the x and y directions. Mathematically, the initial and boundary
 85 conditions are described as follows:

$$\phi(x, y, z, 0) = \sqrt{(x - \frac{L}{2})^2 + (y - \frac{W}{2})^2 + (z - \frac{H}{2})^2 - R} \quad (1)$$

$$\mathbf{u}(x, y, z, 0) = \begin{pmatrix} \frac{2V}{H}(z - \frac{H}{2}) \\ 0 \\ 0 \end{pmatrix}$$

$$\phi(x + L, y, z, t) = \phi(x, y, z, t) \quad \phi(x, y + W, z, t) = \phi(x, y, z, t)$$

$$\mathbf{u}(x, y, H, t) = \begin{pmatrix} V \\ 0 \\ 0 \end{pmatrix} \quad \mathbf{u}(x, y, 0, t) = \begin{pmatrix} -V \\ 0 \\ 0 \end{pmatrix}$$

$$\mathbf{u}(x + L, y, z, t) = \mathbf{u}(x, y, z, t) \quad \mathbf{u}(x, y + W, z, t) = \mathbf{u}(x, y, z, t)$$

86 $\phi(x, y, z, t)$ is a material indicator function which is positive in the “matrix”
 87 fluid and negative in the bubble (or drop) fluid. $\mathbf{u}(x, y, z, t)$ is the velocity.

88 Common dimensionless physical parameters used to describe gas-liquid or
 89 liquid-liquid two-phase flows include the Reynolds (Re), Weber (We) (or Ca (=
 90 We/Re)) and Froude (Fr) numbers. Gas-Liquid and Liquid-Liquid two-phase
 91 flow problems are also determined by the density ratio λ and the viscosity ratio
 92 η . In the present study, the effect of gravity is not considered so that we ignore
 93 the effect of the Fr number.

94 When comparing with previous drop studies, we fix $\lambda = 1$. As a result, (for
 95 $\lambda = 1$) the following dimensionless physical parameters are used to describe the
 96 problem of drop deformation/breakup in shear flow

$$Re = \frac{\rho_m U R}{\mu_m}, \quad Ca = \frac{\mu_m U}{\sigma}, \quad \eta = \frac{\mu_b}{\mu_m} \quad m = \text{matrix fluid} \quad (2)$$

97 U is the velocity scale and σ denotes the surface tension. For the problem of
 98 shear-induced drop deformation and breakup, the velocity is set to $U = \Gamma R$,
 99 where the shear-rate is $\Gamma = 2V/H$. As mentioned in the introduction, most
 100 previous drop studies set $\eta = 1$ (e.g. [22]). Thus, for comparison with previous
 101 drop deformation and breakup problems, we set $\lambda = \eta = 1$ (and also neglect
 102 the effect of gravity so that $g = 0$). On the other hand, in our computations

for bubble deformation, we set the density and viscosity of air to be $\rho_b = 1.2$ kg/m³ and $\mu_b = 1.8 \times 10^{-5}$ Pa·s respectively. We emphasize that for consistency with previous studies ([22, 32, 23, 19, 1]), we computationally examine the deformation and breakup of a bubble in simple linear shear flow as a function of the Re and Ca numbers. That is to say, by setting $g = 0$, we are isolating the effect of only varying Re and Ca on bubble deformation and breakup. In our controlled study, we determine the critical Re_c versus Ca curve in which Re_c corresponds to the threshold of bubble (or drop) breakup. We determine the critical Re_c versus Ca curve for strategic pairs of the density ratio and viscosity ratio.

In our computations, the density of the matrix fluid is fixed at $\rho_m = 1000$ kg/m³. The surface tension at the bubble (drop) interface is $\sigma = 2.5 \times 10^{-2}$ N/m. The values of Re and Ca in our simulations are controlled by changing the values of μ_m and V . For studying bubble deformation and break-up, the density and viscosity ratios satisfy $\lambda = 1.2 \times 10^{-3}$ and $\eta < 1.0 \times 10^{-3}$.

3. Numerical Analysis

3.1. Numerical method and governing equations

Numerical results were obtained using the interface capturing Coupled Level Set and Volume of Fluid (CLSVOF) method [36, 38], which is based on a fixed grid finite volume algorithm. The CLSVOF method is a robust numerical technique that combines some of the advantages of the Volume of Fluid (VOF) method ([11]) and the Level Set (LS) ([37]) method while overcoming their weaknesses. In the VOF method, the Volume Fraction function, F , is used to represent the interface. The values of F correspond to the volume fraction of liquid in a given computational cell. In other words, $F = 0$ when a computational cell contains only gas and $F = 1$ when a computational cell contains only liquid. If $0 < F < 1$, then a computational cell contains the gas-liquid interface. The VOF method has a great advantage over the LS method in that accurate algorithms for advecting F can be applied so that mass/volume is conserved up

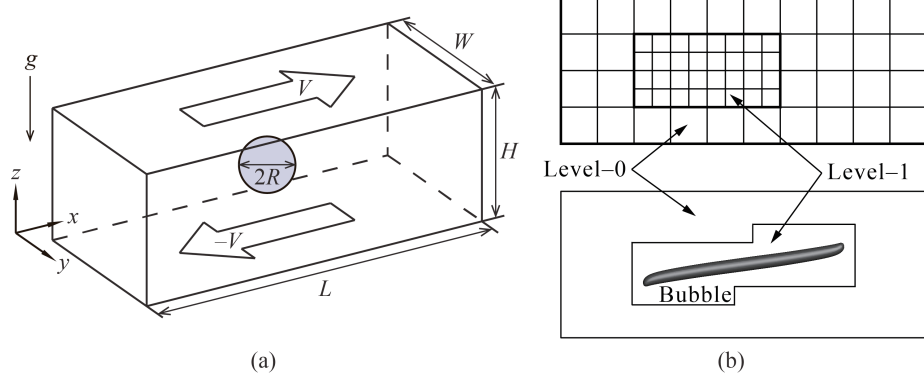


Figure 1: (a) Computational domain schematic for a bubble or drop in shear flow. Gravity is set to zero in our computations in order to isolate the effects of density and viscosity ratios. (b) (*upper panel*) a two-level adaptive mesh refinement (AMR) grid schematic corresponding to one of our simulations; (*lower panel*) snapshot of bubble deformation in simple linear shear flow.

132 to machine precision while still maintaining a sharp representation of the inter-
 133 face. On the other hand, the disadvantage of the VOF method in comparison
 134 to the LS method is that tangled and difficult reconstruction procedures are
 135 required for determining the slope of the piecewise linear VOF reconstructed
 136 interface. In the LS method, the signed distance function ϕ (LS function) is
 137 used to track the interface. The interface is implicitly represented by the set of
 138 points in which $\phi = 0$. Liquid and gas regions are defined as $\phi > 0$ in the liquid
 139 and $\phi < 0$ in the gas, respectively. One of the advantages of the LS method is
 140 that one can track and represent smoothly the interface, but the LS method has
 141 the disadvantage that mass/volume is not explicitly conserved. In the CLSVOF
 142 method, the coupling between the LS function and the VOF function occurs
 143 when computing the normal of the reconstructed interface in the VOF calcu-
 144 lation process and also when assigning the LS function with the exact signed
 145 normal distance to the reconstructed interface in the LS calculation process.
 146 That is to say, the piecewise linear approximation (the volume-of-fluid recon-
 147 struction step) for the VOF method is determined using the unit normal vector
 148 (\mathbf{n}) estimated from information of the LS function. By taking advantage of

149 both methods, the evolution of the liquid-gas interface location can be com-
 150 putationally captured in such a way so that volume/mass is preserved to machine
 151 precision and at the same time, the interface normals and the surface tension
 152 force (which is proportional to the interface curvature) can be straightforwardly
 153 derived from the smooth level set function.

In our studies, the two-phase fluid flow is comprised of air and a viscous
 Newtonian liquid. The Heaviside function, $\mathcal{H}(\phi)$, which is defined as

$$\mathcal{H}(\phi) = \begin{cases} 1 & \phi \geq 0 \\ 0 & \phi < 0 \end{cases} \quad (3)$$

will be used below to distinguish each of the two fluids. A single set of three-dimensional equations governs the motion of both fluids, which are taken to be incompressible, and consists of the continuity equation and the Navier-Stokes equations with surface tension forces:

$$\nabla \cdot \mathbf{u} = 0 \quad (4)$$

$$\frac{\partial \mathbf{u}}{\partial t} + (\mathbf{u} \cdot \nabla) \mathbf{u} = \frac{1}{\rho} \nabla \cdot (-p \mathbf{I} + 2\mu \mathbf{D}) + \mathbf{g} - \frac{\sigma \kappa}{\rho} \nabla \mathcal{H} \quad (5)$$

154 where \mathbf{u} is the velocity vector, t represents time, p is the pressure, \mathbf{I} is the unit
 155 tensor, \mathbf{D} is the rate of deformation tensor ($\mathbf{D} = \frac{1}{2}(\nabla \mathbf{u} + (\nabla \mathbf{u})^T)$), ρ is the
 156 density, μ is the viscosity, κ is the interfacial curvature, and the Heaviside func-
 157 tion $\mathcal{H}(\phi)$ is a function of the level set (LS) function ϕ . The singular Heaviside
 158 gradient term in the right hand side of equation (5) is a body force representing
 159 the surface tension force and is equivalent to specifying that the jump in the
 160 normal stress is equal to $\sigma \kappa$ [39]. The surface tension force expressed by the sin-
 161 gular Heaviside gradient term acts only on the gas-liquid interface. The sharp
 162 interface “Ghost Fluid Method” [17] is used to discretize the gradient of the
 163 Heaviside function as it appears in the surface tension force term. This force,
 164 upon discretization, is only non-zero across cells in which the level set function
 165 changes sign.

166 The interfacial curvature κ is computed with second order accuracy directly
 167 from the volume-of-fluid (VOF) function using the height function technique [34,

¹⁶⁸ 38]. We remark that we get the same results if we were to compute κ directly
¹⁶⁹ from the LS function using the “level set” height function technique.

¹⁷⁰ Since ρ and μ are taken to be constant in each fluid, with a jump at the
¹⁷¹ interface, they can be expressed in terms of the Heaviside function,

$$\rho = \rho_m \mathcal{H} + \rho_b (1 - \mathcal{H}), \quad \mu = \mu_m \mathcal{H} + \mu_b (1 - \mathcal{H}). \quad (6)$$

The subscripts “b” and “m” refer to “drop or bubble” and “matrix fluid”, respectively. To represent the free surface with the CLSVOF method, we must evolve the solution to both the VOF equation for F and the LS equation for ϕ :

$$\frac{\partial F}{\partial t} + (\mathbf{u} \cdot \nabla) F = 0, \quad \frac{\partial \phi}{\partial t} + (\mathbf{u} \cdot \nabla) \phi = 0. \quad (7)$$

¹⁷² In all computations the discretized variables p , ϕ and F are located at cell
¹⁷³ centers and the discrete variable \mathbf{u} is located at cell face centers. Our com-
¹⁷⁴ putations are performed using an overall second-order accurate hydrodynamic
¹⁷⁵ scheme. The spatial discretization uses second-order accurate, slope-limited,
¹⁷⁶ upwind techniques for the nonlinear advective terms. The velocity and pressure
¹⁷⁷ fields are computed using an implicit pressure projection procedure.

¹⁷⁸ The temporal discretization of our numerical method is an operator split
¹⁷⁹ projection method as described by [38]. An outline of our method is as follows
¹⁸⁰ (see [38], section 4, for more details):

¹⁸¹ **Timestep Δt** The timestep is governed by the CFL condition and surface ten-
¹⁸² sion (section 5.7 of [38]):

$$\Delta t < \min_{i,j,k} \left(\frac{\Delta x}{2|U^n|}, \frac{1}{2} \sqrt{\frac{\rho^L}{8\pi\sigma}} \Delta x^{3/2} \right)$$

Step 1. CLSVOF interface advection

$$\phi^{n+1} = \phi^n - \Delta t [\mathbf{u} \cdot \nabla \phi]^n$$

$$F^{n+1} = F^n - \Delta t [\mathbf{u} \cdot \nabla F]^n$$

Step 2. Nonlinear advective force terms

$$\mathcal{A} = [\mathbf{u} \cdot \nabla \mathbf{u}]^n$$

Step 3. Viscosity force

$$\frac{\mathbf{u}^* - \mathbf{u}^n}{\Delta t} = -\mathcal{A} + g\vec{z} - [\nabla p/\rho]^n + \frac{1}{2} \frac{\nabla \cdot (2\mu \mathbf{D}^n) + \nabla \cdot (2\mu \mathbf{D}^*)}{\rho}$$

¹⁸³ **Step 4. Pressure projection and ghost fluid surface tension algorithm**

$$\mathbf{V} = \mathbf{u}^n + \Delta t(-\mathcal{A} + g\vec{z} + \frac{1}{2} \frac{\nabla \cdot (2\mu \mathbf{D}^n) + \nabla \cdot (2\mu \mathbf{D}^*)}{\rho})$$

¹⁸⁴

$$\mathbf{V} = \mathbf{V} - \Delta t \frac{\sigma \kappa(\phi^{n+1})}{\rho} \nabla \mathcal{H}(\phi^{n+1})$$

¹⁸⁵

$$\nabla \cdot \frac{\nabla p}{\rho} = \frac{1}{\Delta t} \nabla \cdot \mathbf{V}$$

¹⁸⁶

$$\mathbf{u}^{n+1} = \mathbf{V} - \Delta t \frac{\nabla p}{\rho}$$

¹⁸⁷ To make efficient use of computational resources, our numerical simulations
¹⁸⁸ utilize an adaptive hierarchy of grids based on a dynamic adaptive mesh refinement
¹⁸⁹ (AMR) technique [35]. Adaptive grids are dynamically adjusted based on
¹⁹⁰ the location of the deforming gas-liquid interface. In the AMR technique the
¹⁹¹ grid resolution is increased in regions near the interface while a coarser grid is
¹⁹² used where the flow is relatively steady. The upper panel of Figure 1(b) displays
¹⁹³ a schematic view of the hierarchical grid structure and the lower panel corre-
¹⁹⁴ sponds to an actual computational example for bubble deformation in simple
¹⁹⁵ linear shear flow. In general, the mesh hierarchy is composed of different levels
¹⁹⁶ of refinement ranging from coarsest $\ell = 0$ (“level-0”) to finest $\ell = \ell_{\max}$ (“level-
¹⁹⁷ ℓ_{\max} ”). The refinement ratio of one grid size ($\Delta x = \Delta y = \Delta z$) to the next finer
¹⁹⁸ level is two so that $\Delta x^{\ell+1} = 0.5\Delta x^\ell$. All computations in this study used an
¹⁹⁹ AMR system with a maximum prescribed level $\ell_{\max} = 1$ (as illustrated in the
²⁰⁰ upper panel of Figure 1(b)). In our adaptive mesh refinement algorithm, the
²⁰¹ velocity in coarse grid cells that neighbor fine grid cells is interpolated from the
²⁰² coarse grid using bilinear interpolation in order to initialize “ghost” fine cells.
²⁰³ Thus, the bilinear interpolation procedure produces interpolated fine grid data
²⁰⁴ as a linear combination of the coarse grid data.

205 *3.2. Validation of the numerical method*

206 Numerical studies reported in this section are presented in order to verify
207 the accuracy of our computational method. First, we compare quantitatively
208 against the steady-state drop deformation results reported by Li et al. [22]. The
209 shape of a deformed drop in simple linear shear flow is described in terms of the
210 Taylor deformation parameter $D = (a - b)/(a + b)$, where a and b are the major
211 and minor axes of the deformed drop. For consistency, we perform numerical
212 simulations using CLSVOF over the same computational domain and grid size
213 used in [22], which has dimensions $L(8R) \times W(4R) \times H(8R)$ (recall that R is
214 the bubble/drop radius) and a level-0 grid size $\Delta x = \Delta y = \Delta z = R/8$; our two-
215 level AMR grid structure also uses a finer level-1 grid size $\Delta x^{\ell=1} = \Delta y^{\ell=1} =$
216 $\Delta z^{\ell=1} = R/16$. Numerical results are listed in Table 1 for D as a function of
217 Re , with $Ca = 0.3$ and $\lambda = \eta = 1$ fixed in every case, obtained with the VOF
218 method used in [22], and also with our CLSVOF algorithm. Table 1 indicates
219 that our numerical results are in good agreement with previous computations
for drop deformation and breakup.

Table 1: Comparison of the Taylor deformation parameter D for a drop as a function of Re ($Ca = 0.3$, $\lambda = \eta = 1$). In all cases, the domain size is $L(8R) \times W(4R) \times H(8R)$, where R is the drop radius. CLSVOF method computations used a two-level AMR computational domain with a level-0 discretization $\Delta x^{\ell=0} = \Delta y^{\ell=0} = \Delta z^{\ell=0} = R/8$ and a level-1 discretization $\Delta x^{\ell=1} = \Delta y^{\ell=1} = \Delta z^{\ell=1} = R/16$.

Reynolds number	0.1	0.5	0.6	0.75
D (Li et al. ([22]))	0.3968	0.45	0.4768	Breakup
D (Our study)	0.3960	0.4570	0.4758	Breakup

220
221 Next, we examine the validation of our computational method in which
222 we compare with the “bubble deformation in simple linear shear flow” results
223 reported by Muller-Fischer et al. [23]. Muller-Fischer et al. [23] experimentally
224 inquired into the bubble deformation under the condition of $Re \approx 0$. In our
225 study, we computed the bubble deformation on a computational domain with

226 dimensions $L(12R) \times W(6R) \times H(6R)$ and a computational grid in which the
 227 finest level grid size was $\Delta x^{\ell=1} = \Delta y^{\ell=1} = \Delta z^{\ell=1} = R/16$. Computations
 228 were performed for the conditions of $Ca = 0.96$ and $Ca = 1.63$ with $Re \approx 0$
 229 ($Re = 5.0 \times 10^{-4}$), $\lambda = 1.2 \times 10^{-3}$ and $\eta \leq 1.2 \times 10^{-6}$. The parameters
 230 that we have prescribed are consistent with the experimental conditions by
 231 Muller-Fischer et al. [23]. Comparisons of our numerical results and previous
 232 experimental results ([23]) are tabulated in Table 2. Additionally, in Table 2,
 233 we also list experimental results with the condition of $Re \approx 0$ and $\lambda \approx \eta \approx 0$
 234 by Rust and Manga ([32]). These experimental values by Rust and Manga
 235 ([32]) were obtained from the graph showing the relation of D vs Re ([32]).
 236 As is clear from Table 2, our numerical results predicted larger values of D
 237 than experimental ones reported by Muller-Fischer et al. [23]. Nevertheless,
 238 we found that our numerical results are very close to the experimental results
 239 by Rust and Manga ([32]), which emphasizes the intrinsic difficulties associated
 240 with experimental investigations of bubble dynamics, even in simple linear shear
 241 flow. These comparisons suggest that our computational method is effective and
 242 robust at reproducing bubble dynamics in simple linear shear flow.

Table 2: Comparison of D for a bubble as a function of Ca ($Re \approx 0$, $\lambda \approx \eta \approx 0$). In all cases, the domain size is $L(12R) \times W(6R) \times H(6R)$. CLSVOF computations used a two-level AMR computational domain with a level-0 discretization $\Delta x^{\ell=0} = \Delta y^{\ell=0} = \Delta z^{\ell=0} = R/8$ and a level-1 discretization $\Delta x^{\ell=1} = \Delta y^{\ell=1} = \Delta z^{\ell=1} = R/16$.

Capillary number	0.96	1.63
D (Muller-Fischer et al. ([23]))	0.37	0.58
D (Rust and Manga ([32]))	0.71 ± 0.05	0.81 ± 0.02
D (Our study $\Delta x^{\ell=1} = R/16$)	0.63	0.75

243 Finally, we present a comparison with numerical results for drop breakup
 244 reported in [31]. Figure 2 demonstrates drop breakup with pinch-off behavior
 245 for three Re and Ca conditions and with constant values of $\lambda = \eta = 1$ for all
 246 cases. The three cases that we consider correspond to (a) $Re = 10$, $Ca = 0.16$,

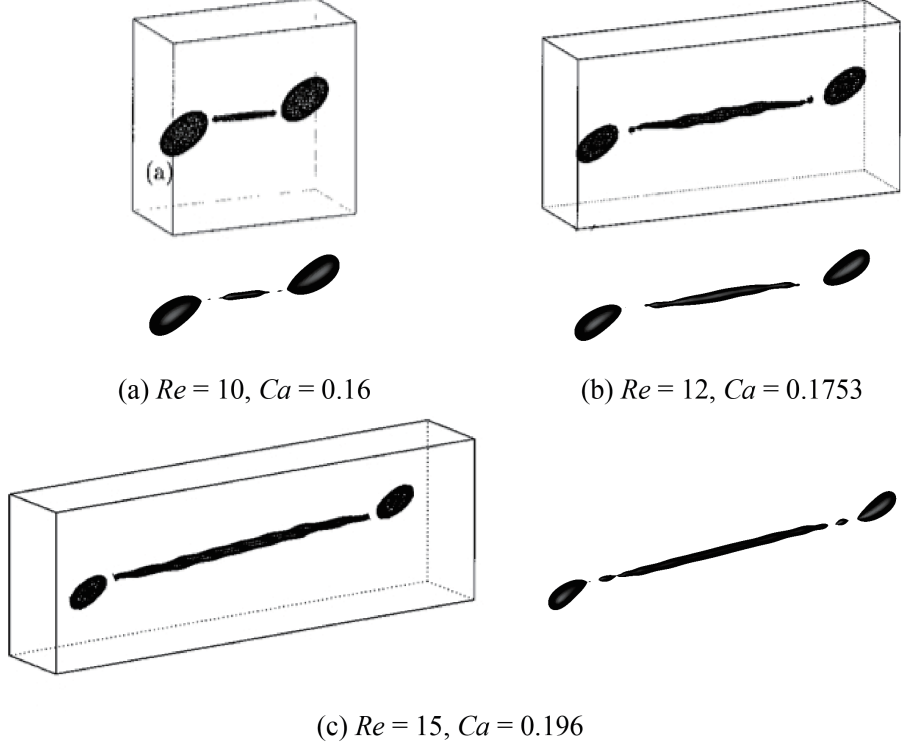


Figure 2: Comparison with results reported in [31] (shown in boxes) for drop breakup in shear flow. In [31], the computational domain dimensions were $W = 4R$, $H = 8R$, and L was varied depending on the Re and Ca conditions. The grid size in [31] was set to $\Delta x = \Delta y = \Delta z = R/8$. Reprinted with permission from reference [31]. Copyright 2001, AIP Publishing. Results obtained with our CLSVOF algorithm, corresponding to each case in reference [31], are shown outside boxes. The CLSVOF method used a two-level AMR computational domain with a level-0 discretization $\Delta x^{\ell=0} = \Delta y^{\ell=0} = \Delta z^{\ell=0} = R/8$ and a level-1 discretization $\Delta x^{\ell=1} = \Delta y^{\ell=1} = \Delta z^{\ell=1} = R/16$. The onset of drop breakup is demonstrated for (a) $Re = 10, Ca = 0.16$, (b) $Re = 12, Ca = 0.1753$, and (c) $Re = 15, Ca = 0.196$. For all three Re and Ca conditions, $\lambda = \eta = 1$.

²⁴⁷ (b) $Re = 12, Ca = 0.1753$, and (c) $Re = 15, Ca = 0.196$, and which are
²⁴⁸ illustrated in Figures 2(a)-(c), respectively. The results reported in [31], which
²⁴⁹ were obtained with a VOF method, are shown inside boxes while results obtained
²⁵⁰ with our CLSVOF approach are displayed outside boxes. In the computations
²⁵¹ presented in [31], the dimensions $W = 4R$ and $H = 8R$ were fixed, while L was

252 changed depending on Re and Ca conditions, and the grid size was set to $\Delta x =$
253 $\Delta y = \Delta z = R/8$. To compare with their results, we performed simulations with
254 the CLSVOF method over a two-level AMR computational domain of the same
255 dimensions and the same level-0 discretization: $\Delta x^{\ell=0} = \Delta y^{\ell=0} = \Delta z^{\ell=0} =$
256 $R/8$; we set the finer level-1 grid size $\Delta x^{\ell=1} = \Delta y^{\ell=1} = \Delta z^{\ell=1} = R/16$. The
257 results shown in Figure 2 verify that our numerical approach can reproduce the
258 same drop breakup behavior presented in [31]. Slight differences between the
259 results can be attributed to the increased resolution used in our study in the
260 level-1 grid around the elongated drop.

261 The numerical validation studies performed in this section and the follow-
262 ing section demonstrate that our numerical method can reliably determine the
263 transition regions at which shear-induced bubble or drop deformation leads to
264 breakup. We remark that in the next section, we demonstrate that we can ex-
265 pect an error of 3% for predicting the transition to break-up. The analysis in
266 this section and the following also demonstrate that the error is reduced by a
267 factor of 2 each time the grid is refined by a factor of 2. Also, we refer the reader
268 to [24] in which we apply our CLSVOF method for bubble formation problems.

269 *3.3. Consideration of domain and grid sizes*

270 *3.3.1. Selecting the appropriate domain size*

271 The computational domain size used in numerical studies can affect the
272 behavior of drop deformation and breakup. Referring to Figure 1(a), with an
273 appropriately large domain length L and a fixed width $W = 4R$, the effect of the
274 height H on drop behavior was examined in [22] for Stokes flows and various
275 Ca conditions and in [19] for $Re = 1$ and $Ca = 0.27$. Other related studies
276 investigated drop breakup sensitivity [29] and drop deformation sensitivity [30]
277 with respect to the entire domain size.

278 Here we investigate the drop dynamics sensitivity to domain size around
279 the critical Reynolds number $Re_c = 0.75$. Specifically, we consider domain size
280 sensitivity for the condition of $Re = 0.75$, $Ca = 0.3$, and $\lambda = \eta = 1$, which is a
281 condition used in the comparison studies of the previous section. As shown in

Table 3: Comparison of the Taylor deformation parameter D for a drop as a function of domain size ($Re = 0.75$, $Ca = 0.3$, $\lambda = \eta = 1$). CLSVOF method computations used a two-level AMR computational domain with a level-0 discretization $\Delta x^{\ell=0} = \Delta y^{\ell=0} = \Delta z^{\ell=0} = R/8$ and a level-1 discretization $\Delta x^{\ell=1} = \Delta y^{\ell=1} = \Delta z^{\ell=1} = R/16$.

System	Domain size ($L \times W \times H$)	D
System 1	$8R \times 4R \times 8R$	Breakup
System 2	$12R \times 4R \times 8R$	Breakup
System 3	$8R \times 4R \times 6R$	0.541
System 4	$8R \times 6R \times 6R$	0.466
System 5	$8R \times 8R \times 8R$	0.460
System 6	$8R \times 16R \times 16R$	0.460

282 Table 1, the drop breaks up for the condition of $Re = 0.75$ and $Ca = 0.3$ with
 283 a domain size of $L(8R) \times W(4R) \times H(8R)$. Results for domain size sensitivity
 284 for six domain systems, all of which use a level-1 grid size $\Delta x^{\ell=1} = \Delta y^{\ell=1} =$
 285 $\Delta z^{\ell=1} = R/16$, are tabulated in Table 3. Note that the domain size used in the
 286 comparison study (Table 1) corresponds to System 1.

287 The results in Table 3 suggest that drop deformation is promoted when we
 288 use a domain size with $W = 4R$. In contrast, the drop does not break up and
 289 becomes stable with a deformed shape if we set L large enough and $W \geq 6R$ and
 290 $H \geq 6R$. Since the value of D for the domain size $L(8R) \times W(6R) \times H(6R)$ differs
 291 by only 1.3% with the value for the domain size of $L(8R) \times W(16R) \times H(16R)$,
 292 in the results that follow we set the width to $W = 6R$ and the height to $H = 6R$
 293 to minimize the number of computational grid nodes along those directions. To
 294 determine the critical Reynolds number Re_c (with $Ca = 0.3$), we consider a
 295 domain size of $L(24R) \times W(6R) \times H(6R)$, and we find that the drop reaches a
 296 stable state with deformation parameter $D=0.549$ for $Re = 1.0$, while a value
 297 of $Re = 1.1$ leads to drop breakup.

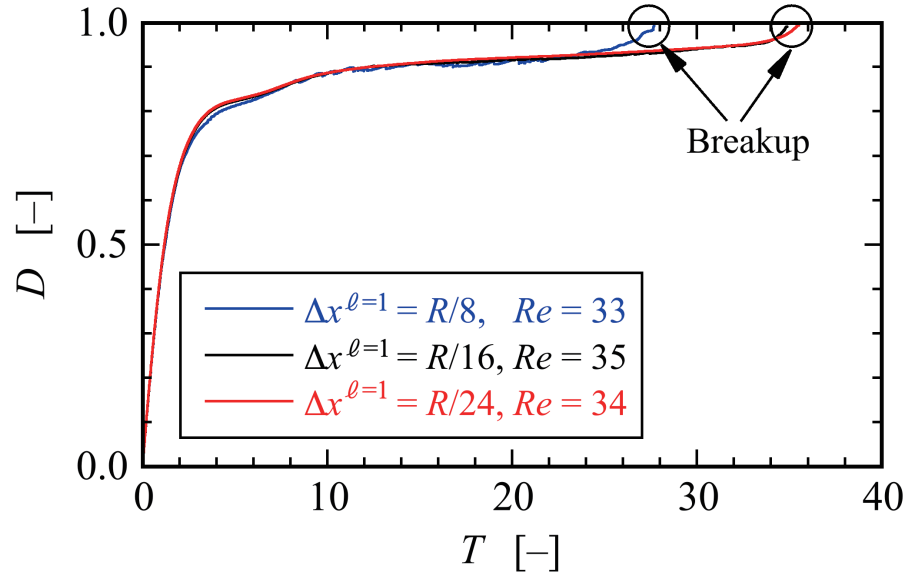


Figure 3: Time evolution of the deformation parameter D versus dimensionless time $T = \Gamma t$ for a bubble, obtained with three grid systems at different resolutions. All three resolutions use a two-level AMR grid with an effective fine resolution grid size $\Delta x^{\ell=1} = \Delta y^{\ell=1} = \Delta z^{\ell=1}$. The evolution of D using the first system, where $\Delta x^{\ell=1} = R/8$, is shown in blue and it predicts that bubble breakup occurs at a Reynolds number $Re = 33$. The evolution of D using the second system, where $\Delta x^{\ell=1} = R/16$, is shown in black and it predicts that bubble breakup occurs at a Reynolds number $Re = 35$. Results with the third system, shown in red, use $\Delta x^{\ell=1} = R/24$, and they predict that breakup occurs at $Re = 34$. The capillary number corresponding to these results is $Ca = 1.0$. ($\lambda = 1.2 \times 10^{-3}$, $\eta < 1.0 \times 10^{-3}$)

298 3.3.2. *Selecting the appropriate grid size*

299 The grid size and adaptive meshing strategy that we adopt is chosen in order
300 to answer the research question as to the conditions which determine whether
301 a bubble in shear flow will break-up or not. In such a case, we must accurately
302 capture the balance of forces with respect to the (non-local) force exerted from
303 the wall driven flow acting against the interfacial surface tension force. The
304 accuracy of the “Critical Reynolds Number” depends on the largest Taylor De-
305 formation parameter D that is supported by the grid (see e.g. Figures 8 and
306 11). As we report here, we have found that as long as the grid size is fine enough
307 to support a Taylor Deformation parameter $D < 0.95$, then the transition re-
308 gion (i.e. “Critical Reynolds number”) (see Figures 3 and 12) will be captured
309 with a tolerance of three percent. The simulation time becomes impractical if
310 we were to try to further improve the “critical Reynolds number” accuracy. A
311 smaller tolerance would necessitate a larger supported Deformation parameter
312 D which would in turn necessitate a higher aspect ratio computational domain,
313 increased droplet surface area at break-up, increased number of time steps, and
314 higher resolution for representing the drop/bubble at its thinnest point.

315 We make the distinction between our present research, and the research
316 found in the work of Zang, Ni, and Magnaudet[46, 47] on predicting the condi-
317 tions for bubble mergers. Even in the most extreme cases for mergers, the largest
318 Deformation parameter never exceeds 0.4 in [46]. In summary, our gridding re-
319 quirements necessitate grid points distributed relatively evenly throughout the
320 computational domain when a bubble is stretched to a $D = 0.9$ Deformation,
321 whereas in [46] the gridding strategy necessitates a more localized strategy.

322 The numerical results presented in this and the previous section used a
323 finest-level grid size set to $\Delta x^{\ell=1} (= \Delta y^{\ell=1} = \Delta z^{\ell=1}) = R/16$. To verify the
324 adequacy of this grid resolution, we present grid refinement results for a bubble
325 breakup simulation with $Ca = 1.0$, which corresponds to the most deformable
326 and stretchable bubble case considered in our numerical studies. We use three
327 different grid systems, (i) $\Delta x^{\ell=1} = R/8$, (ii) $\Delta x^{\ell=1} = R/16$, and (iii) $\Delta x^{\ell=1} =$

328 $R/24$, in order to determine Re_c . Figure 3 shows the time evolution of the
 329 deformation parameter D over time for the three grid systems; the x -axis is a
 330 dimensionless time defined by $T = \Gamma t$ and the y -axis is D . The results show that
 331 bubble breakup occurs at $Re_c = 35$ for the grid system with $\Delta x^{\ell=1} = R/16$,
 332 while the finer computational grid with $\Delta x^{\ell=1} = R/24$ predicts a critical value of
 333 $Re_c = 34$. For the $\Delta x^{\ell=1} = R/8$ results, it is clear that the $R/8$ resolution is too
 334 coarse in order to capture the proper break-up time, albeit the critical Reynolds'
 335 number, $Re_c = 33$, was still close to the finer grid resolution cases. Note that
 336 although the time evolution of D for the two finer resolution systems ($R/16$ and
 337 $R/24$) is consistent between the two, (the predicted critical Reynolds numbers
 338 differ by $\sim 3\%$), the computational time using the grid system with $\Delta x^{\ell=1} =$
 339 $R/24$ was more than 6 times longer than the one based on the coarser system
 340 with $\Delta x^{\ell=1} = R/16$. We remark that in our search for Re_c , we considered a wide
 341 range of values of Ca and we found it necessary to use a large L ($\sim 24R$) since
 342 for certain shear flows the bubble can stretch significantly without breaking up.
 343 Nevertheless, for the conditions presented in this section, the results indicate
 344 that our numerical approach, even with a finest-level resolution set to $\Delta x^{\ell=1} =$
 345 $R/16$, is capable of accurately reproducing bubble deformation and breakup
 346 without sacrificing any essential dynamical features.

347 **4. Results and Discussion**

348 *4.1. Drop deformation and breakup*

349 To illustrate the differences in deformation and breakup between a drop
 350 and a bubble around critical conditions, we first present numerical results for
 351 drop deformation. The time evolution of drop deformation and breakup in
 352 simple linear shear flow for two conditions is shown in Figure 4; the first case,
 353 shown in Figure 4(a), uses $Ca = 0.3$ and $Re = 1.0$, while the second case,
 354 depicted in Figure 4(b), uses $Ca = 0.3$ and $Re = 1.1$. Using a domain size
 355 of $L(24R) \times W(6R) \times H(6R)$, in the case with $Re = 1.0$, the drop gradually
 356 deforms and finally attains a stable deformed state with $D = 0.549$. Over the

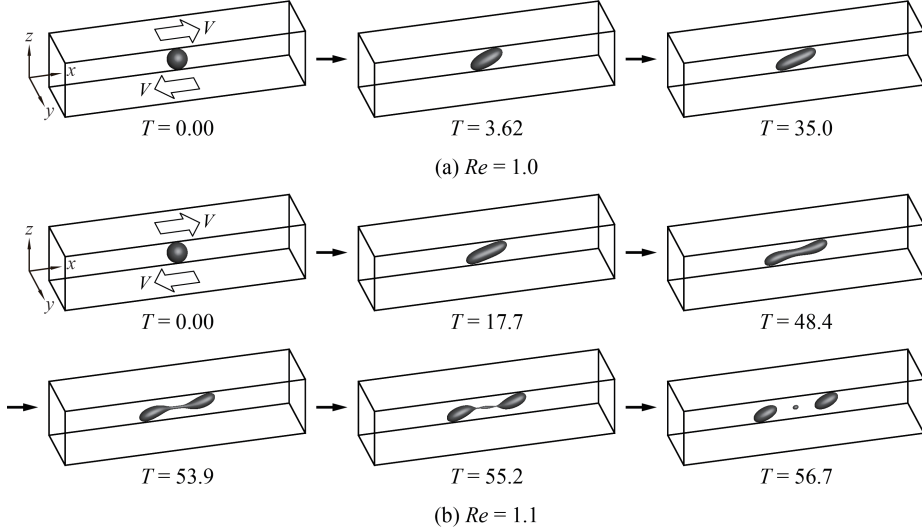


Figure 4: Time evolution of drop deformation and breakup in shear flow at the condition of $Ca = 0.3$ with (a) $Re = 1.0$ and (b) $Re = 1.1$. The “drop” critical Reynolds number corresponding to $Ca = 0.3$ is $1.0 < Re_c < 1.1$. ($\lambda = \eta = 1.0$)

same domain, for the case with $Re = 1.1$, the “mother” drop elongates over time and the volume at the ends of the deforming drop expands; that is, both ends of the drop become bulb-shaped. As time progresses, particularly over the time interval $48.4 \leq T \leq 55.2$, a thread-bridge forms between the bulbous ends and the thread-bridge becomes thinner. Finally, at around the dimensionless time $T \sim 56.7$, the mother drop breaks up, forming two “daughter” drops through the pinch off; one satellite drop is also generated between the pinched off daughter drops.

4.2. Bubble deformation and breakup

Next we present numerical results that illustrate the conditions that lead to bubble deformation without breakup as well as conditions where the bubble deforms and ultimately breaks up. The time evolution of shear-induced bubble deformation without breakup at the condition of $Ca = 0.3$ and $Re = 92$ is depicted in Figure 5 and the bubble breakup process with flow condition of $Ca = 0.3$ and $Re = 93$ is illustrated in Figure 6. The results indicate that

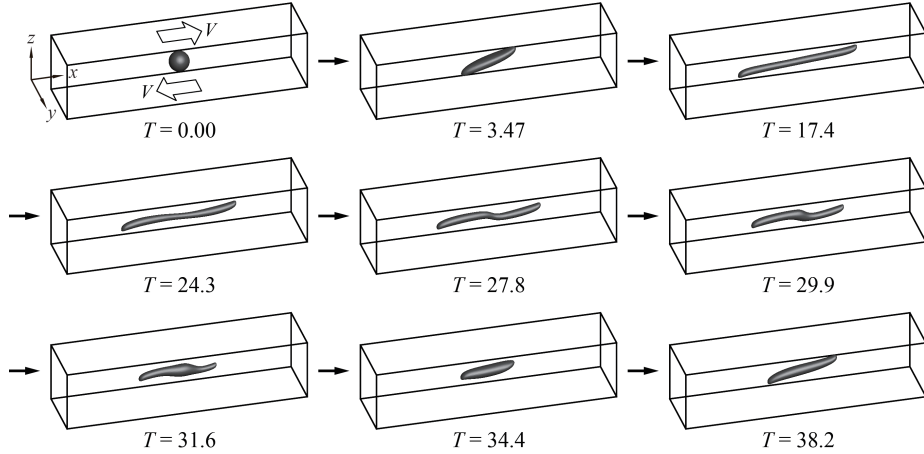


Figure 5: Time evolution of bubble deformation in shear flow at the condition of $Ca = 0.3$ and $Re = 92$. The “bubble” critical Reynolds number corresponding to $Ca = 0.3$ is $92 < Re_c < 93$. In contrast to the drop deformation case, when Re is slightly below Re_c (See Figure 4 $Re = 1.0$ for the drop case), the bubble shape will not reach a steady shape, instead the bubble shape alternates between the shapes “slightly stretched” ($T = 3.47$), fully stretched and “doglegged” ($T = 27.8$) and “almost” back to the original “slightly stretched” case ($T = 34.4$). ($\lambda = 1.2 \times 10^{-3}$, $\eta < 1.0 \times 10^{-3}$)

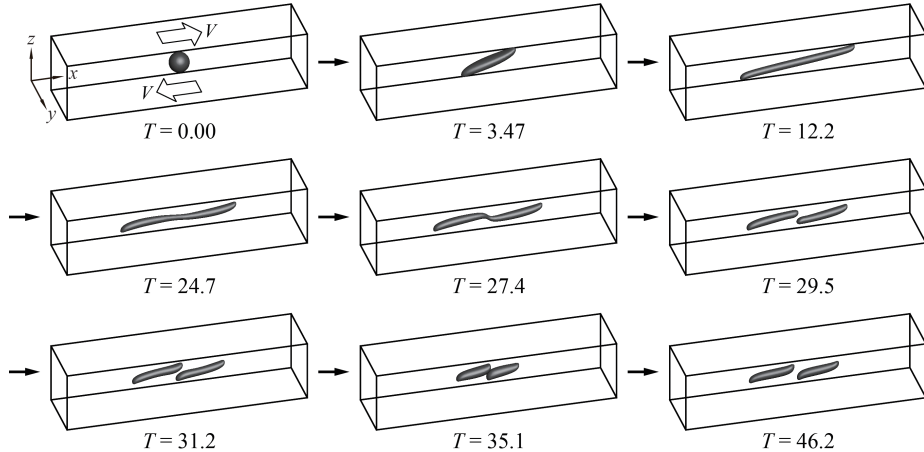


Figure 6: Time evolution of bubble deformation in shear flow at the condition of $Ca = 0.3$ and $Re = 93$. The “bubble” critical Reynolds number corresponding to $Ca = 0.3$ is $92 < Re_c < 93$. ($\lambda = 1.2 \times 10^{-3}$, $\eta < 1.0 \times 10^{-3}$)

372 the critical Reynolds number is approximately $Re_c = 93$ (with $Ca = 0.3$).
373 A comparison with the drop breakup dynamics presented in Section 4.1 and
374 the corresponding processes for bubble deformation and breakup exhibit very
375 distinct features. First, we note that a relatively large shear force magnitude is
376 required for bubble breakup ($\lambda = 1.2 \times 10^{-3}$, $\eta < 1.0 \times 10^{-3}$) compared with the
377 case of the drop ($\lambda = \eta = 1$). Then, for the same value of $Ca = 0.3$, the critical
378 Reynolds number for the bubble is around 85 times larger than that for the
379 drop. Focusing on the bubble dynamics with no-breakup (Figure 5), the results
380 show that the bubble is largely elongated in the x -direction at the early stages
381 ($T \leq 24.3$) of bubble deformation, but the bubble does not develop the bulb-
382 like shape (large volume areas) at both ends present in the drop deformation
383 process. It is also evident that the ends of the deforming bubble develop cusped
384 shapes under the influence of the strong shear flow. A noteworthy feature for
385 the non-breaking bubble is that it does not settle into a deformed stable state
386 as in the case of drop deformation presented in Figure 4(a). After an initial
387 elongation process, the bubble enters a shrinking phase ($T = 27.8$) where the
388 doglegged shape formed at the center of the bubble returns to a smaller deformed
389 shape ($T = 34.4$) that is similar to its earlier shape ($T = 3.47$). However, when
390 we compare the early deformed bubble shape at $T = 3.47$ with the shape at
391 $T = 34.4$, it is clear that the shapes are not identical. Following the shrinking
392 phase, the bubble begins to stretch again ($T = 38.2$) and the bubble oscillates
393 between its elongated shape and shortened geometry.

394 For the case of bubble breakup (Figure 6), we observe that the deformation
395 process is almost the same as the no-breakup case until the doglegged shape
396 is formed at $T \sim 27.4$. The bubble finally breaks during the time interval
397 $27.7 \leq T \leq 29.5$. For a closer examination of the bubble breakup process,
398 a detailed panel of cross-sectional slices in the xz -plane through the bubble
399 shape center is presented in Figure 7. The images displayed in Figure 7, which
400 are taken at shorter time intervals than those shown in Fig. 6, reveal that the
401 bubble breaks up into two daughter bubbles due to the pinch off at the thread-
402 bridge part of the doglegged shape during the shrinking process ($T = 28.5 \sim$

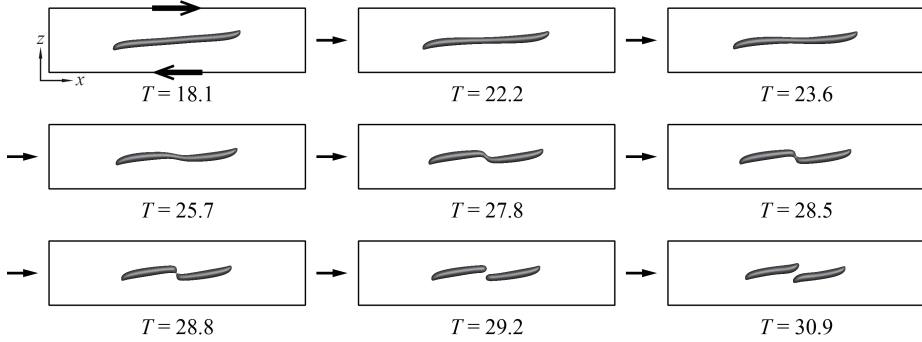


Figure 7: Detail of bubble breakup process in shear flow at the condition of $Ca = 0.3$ and $Re = 93$. The “bubble” critical Reynolds number corresponding to $Ca = 0.3$ is $92 < Re_c < 93$. ($\lambda = 1.2 \times 10^{-3}$, $\eta < 1.0 \times 10^{-3}$)

28.8). After breaking up, the two daughter bubbles migrate to the center: the left daughter bubble moves toward the right-side of the domain and the right daughter bubble moves to the left side (see results for $T = 29.5 \sim 35.1$ in Figure 6 and for $T = 28.8 \sim 30.9$ in Figure 7). The two daughter bubbles then momentarily congregate near the domain center ($T = 35.1$ in Figure 6), before they slowly start to separate: the left daughter bubble moves to the left and the right daughter bubble moves to the right ($T = 46.2$ in Figure 6). The results clearly demonstrate that the bubble breakup process is markedly different from the analogous drop breakup process.

4.3. Shear stress acting on the bubble

In the previous section, the appearance of bubble deformation and breakup was discussed. It is expected that a large deformation and breakup of the bubble are closely related to the state of shear stress acting on the bubble. Figure 8 shows the shear stress profile around a bubble for two Reynolds numbers under the condition of $Ca = 0.3$: Reynolds number equal to 50 and 93. The shear stress profile on the left corresponds to the case of $Re = 50$ and the right side shows the shear stress profile for the case of $Re = 93$. The normalized shear stress, $\tau^* = \tau/\tau_0$, is defined as a ratio of the local shear stress $\tau = \mu_m \sqrt{2\mathbf{D} : \mathbf{D}}$

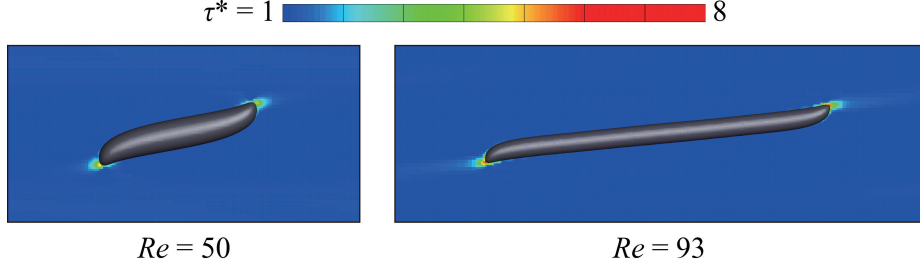


Figure 8: Normalized shear stress τ^* around a bubble for two Reynolds numbers under the condition of $Ca = 0.3$. The left image shows the shear stress profile at $Re = 50$ and the right image at $Re = 93$.

and the apparent shear stress $\tau_0 = \mu_m \Gamma$. In this study, for a given Ca condition, the same value of τ_0 is used regardless of Re .

For the case of $Re = 50$, the bubble reaches a deformed stable state.

As observed in previous sections, when the value of Re is slightly below the critical Re condition, the bubble does not settle into a deformed stable state but instead alternates in an elongation and contraction process. In comparison to the $Re = 50$ case on the left, the right image in Fig. 8 ($Re = 93$) shows a higher shear stress profile near the bubble endpoints as it undergoes an elongation state in the process toward breakup. The value of the maximum shear stress for the case of $Re = 50$ is $\tau^* \approx 6$ and the maximum shear stress for the case of $Re = 93$ at the moment shown in Fig. 8 has the value of $\tau^* \approx 8$. The shear stress profile in Fig. 8 (color contour) is drawn in the range from $\tau^* = 1$ to $\tau^* = 8$, but, for emphasis, shear stress regions with $\tau^* \geq 6$ are illustrated in red. As can be seen in the figure, the strongest shear stresses are concentrated on the ends of the bubble for both Re conditions. This indicates that the strong shear stresses acting on the ends of the bubble are responsible for much of the bubble stretching. It is important to note that the magnitude of the shear stress acting on the ends of the bubble for the case of $Re = 93$ is much larger than that for the case of $Re = 50$.

We also observe that the shear stress *inside* the bubble was very small relative to that of the matrix fluid due to very small density and viscosity of the bubble.

442 Since the force of strong shear stresses acting on the ends of the bubble is
443 difficult to transfer across the interface, as a consequence, a sufficiently large Re
444 condition is required for large bubble deformations.

445 In summary, what we discover is that for the Reynolds number sufficiently below
446 the critical value, a relatively quick unsteady elongation period gives way to a
447 steady state (with no break up). On the other hand for Reynolds number *close*
448 to the critical Reynolds number, there is a prolonged, unsteady, elongation
449 period, in which periodic motion is observed and the deformation parameter
450 D is close to one. The “vacillating” behavior cannot last forever, ultimately
451 (perhaps stochastically!), the bubble will either settle down or break. We assert
452 that regardless of the outcome, this vacillating behaviour will always occur in
453 close proximity to the critical Reynolds’ number. In other words, regardless of
454 the outcome, we claim, using the grid resolution of $R/16$, that one is assured
455 of being within 3 percent of the critical Reynolds number (see Figure 3). In
456 fact, we hypothesize that there will *always* be “vacillating” behavior if one is
457 sufficiently close to the critical Reynolds number. i.e. given an almost infinite
458 supply of computational resources, as one hones in closer and closer to the
459 critical Reynolds number, a “tug of war” will be observed between the surface
460 tension force trying to pull the bubble together versus the wall driven shear
461 stress trying to pull the bubble apart.

462 *4.4. Velocity field outside and inside the breaking bubble*

463 In this section, we consider the fluid flow velocity field outside and inside the
464 bubble during the shear-induced breakup process. Figure 9 shows the velocity
465 fields outside and inside the bubble at cross-sectional slices in the xz -plane
466 for a flow condition of $Ca = 0.3$ and $Re = 93$. Regions around the bubble
467 where there is a higher density of velocity vectors correspond to the level-1 grid
468 portion of the AMR structure. The simulation results show that the velocity
469 field inside the bubble is particularly distinct from the surrounding flow field
470 in the exterior of the bubble. The cross-sections at $T = 12.2$ and $T = 18.1$,
471 taken during the elongation phase, show how shear forces at the lower and

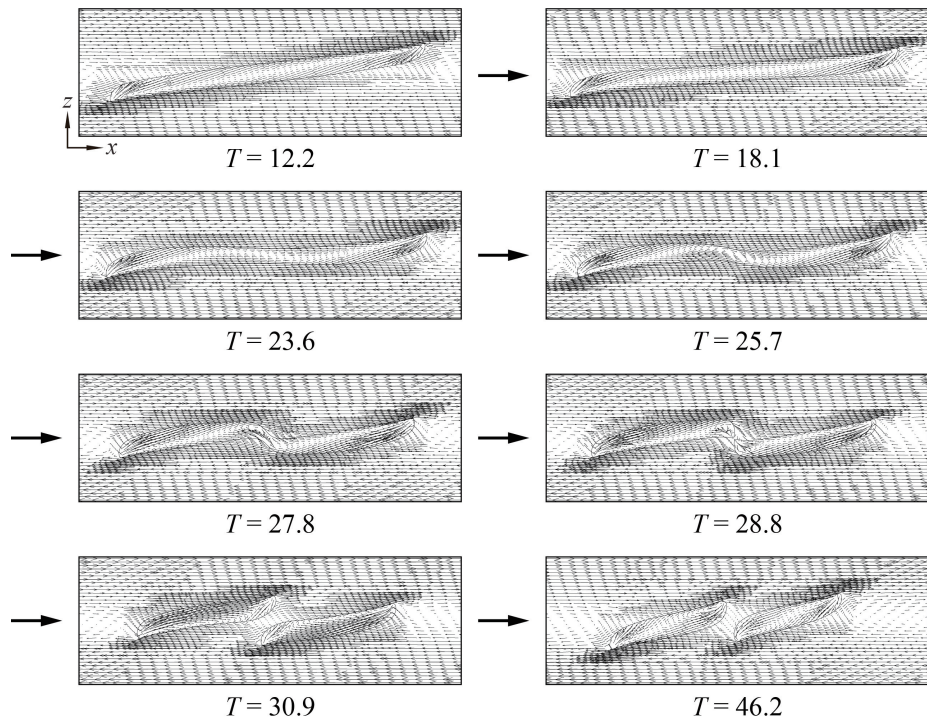


Figure 9: Fluid velocity field outside and inside the breaking bubble in shear flow at the condition $Ca = 0.3$ and $Re = 93$. The “bubble” critical Reynolds number corresponding to $Ca = 0.3$ is $92 < Re_c < 93$. ($\lambda = 1.2 \times 10^{-3}$, $\eta < 1.0 \times 10^{-3}$)

472 upper halves of the bubble act along the bottom and top surfaces, respectively,
473 to deform the interface. Near the left and right edges of the bubble, inward
474 interior flows (that point toward the bubble center) begin to develop. Strong
475 shearing forces in the exterior near the bottom-left-end and top-right-end of
476 the bubble interact with the interior flow field through the boundary to create
477 cusped shapes at the bottom-left and top-right ends of the bubble while the
478 interface is laterally elongated in the x -direction. During the shrinking process,
479 which occurs for $23.6 \leq T \leq 27.8$, inward flows within the bubble extend over
480 a wider region and are no longer localized near the bubble edges. Then, we
481 observe that circulating flows form at the thread-bridge part of the doglegged
482 bubble shape over the time interval [25.7, 27.8]. During the breakup process
483 ($T \sim 28.8$), higher-intensity inward flows are formed inside the bubble, near the
484 pinch off region, that are naturally larger than the surrounding interior flows
485 and which are inextricably associated with the bubble migration illustrated in
486 Figs. 6 and 7. As time proceeds further ($T = 46.2$), distinct inward flows are
487 formed inside the daughter bubbles; the bubbles then begin their migration
488 toward the side walls. Considering the left daughter bubble, for example, we
489 see that the mechanism responsible for this movement results from larger shear
490 forces acting on the bottom-left end than those in the top-left end.

491 *4.5. Effect of surface tension on bubble deformation and breakup*

492 In previous sections, we considered numerical simulations of bubble deforma-
493 tion and breakup with a Capillary number $Ca = 0.3$. Here, we examine similar
494 bubble dynamics with $Ca = 0.8$ and we also investigate the effect of interfacial
495 tension on bubble deformation and breakup. Using $Ca = 0.8$ for both cases,
496 Figures 10 and 11 present the time evolution of shear-induced bubble deforma-
497 tion and breakup with $Re = 42$ and $Re = 43$, respectively. We note that the
498 bubble critical Reynolds number is around $Re_c \approx 43$, whereas $Re_c \approx 0$ for the
499 corresponding case of the drop with $\lambda = \eta = 1$ (see e.g. [22]). Note that Re_c for
500 $Ca = 0.8$ is smaller than that for the condition of $Ca = 0.3$ since the bubble at
501 $Ca = 0.8$ is more elastic due to the weaker effect of surface tension in this case.

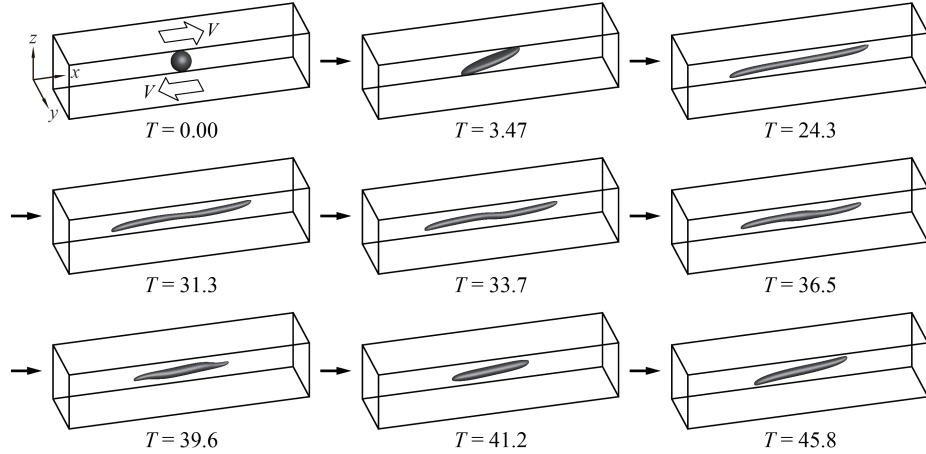


Figure 10: Time evolution of bubble deformation in shear flow at the condition of $Ca = 0.8$ and $Re = 42$. The “bubble” critical Reynolds number corresponding to $Ca = 0.8$ is $42 < Re_c < 43$. ($\lambda = 1.2 \times 10^{-3}$, $\eta < 1.0 \times 10^{-3}$)

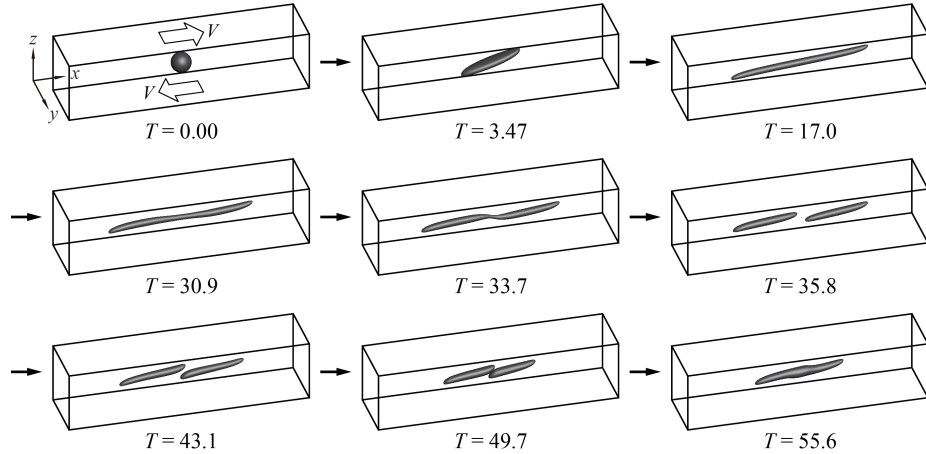


Figure 11: Time evolution of bubble deformation in shear flow at the condition of $Ca = 0.8$ and $Re = 43$. The “bubble” critical Reynolds number corresponding to $Ca = 0.8$ is $42 < Re_c < 43$. ($\lambda = 1.2 \times 10^{-3}$, $\eta < 1.0 \times 10^{-3}$)

502 The results shown in Figs. 10 and 11 indicate that the bubble deformation and
503 breakup process for the condition of $Ca = 0.8$ is analogous to that for $Ca = 0.3$.
504 For the case of bubble deformation without breakup (Fig. 10), the bubble ini-
505 tially assumes a long elongated shape along the x -direction at around $T = 24.3$.
506 The bubble then enters a compression stage over the time interval [31.3, 41.2]
507 and subsequently starts to elongate again at $T = 45.8$. On the other hand, for
508 the case of bubble breakup (Fig. 11), an initial elongation phase is followed by
509 a doglegged shape formation at $T = 33.7$. After that, the bubble ruptures from
510 the thread-bridge part of the doglegged shape and two daughter bubbles are
511 produced ($T = 35.8$). The two daughter bubbles formed after breakup move to
512 the central area ($T = 49.7$) as in the case of $Ca = 0.8$ and $Re = 93$, but the two
513 bubbles eventually coalesce in a region approximately centered in the computa-
514 tional domain ($T = 55.6$). We note that in a real experimental setting, bubbles
515 may coalesce after breaking up due to slight deviations of flow conditions and
516 states. Although the process of bubble deformation and breakup for flow con-
517 ditions with $Ca = 0.3$ and $Ca = 0.8$ are similar, a pronounced difference is that
518 the bubble for $Ca = 0.8$ is more elongated and slender than that for $Ca = 0.3$
519 due to the smaller effect of surface tension for $Ca = 0.8$.

520 Table 4 lists, for representative Ca values, the corresponding critical Reynolds
521 number, Re_c , for shear-induced bubble breakup. The data in Table 4 corre-
522 sponds to $\lambda = 1.2 \times 10^{-3}$, $\eta < 1.0 \times 10^{-3}$, $0.3 < Ca < 1$, and the initial/boundary
523 conditions are given by (1). The results in Table 4 indicate that sufficiently large
524 shear forces are required for bubble breakup even for large Capillary numbers.
525 In Figure 12 we plot the smooth interpolant of the data given in Table 4 and
526 make the hypothesis that given a new data point, (Ca, Re) , shear induced bub-
527 ble break up will occur if the point (Ca, Re) is above the given critical curve,
528 and the bubble will not break if the (Ca, Re) pair is below the critical curve.
529 For comparison, a critical curve for the drop with $\lambda = \eta = 1$ is also indicated
530 in Fig. 12. The inclusion of breakup and no-breakup critical curves, for both
531 the drop and the bubble, will facilitate future identification of Re_c numbers—
532 and thus a more complete general critical curve—for a wide range of high Ca

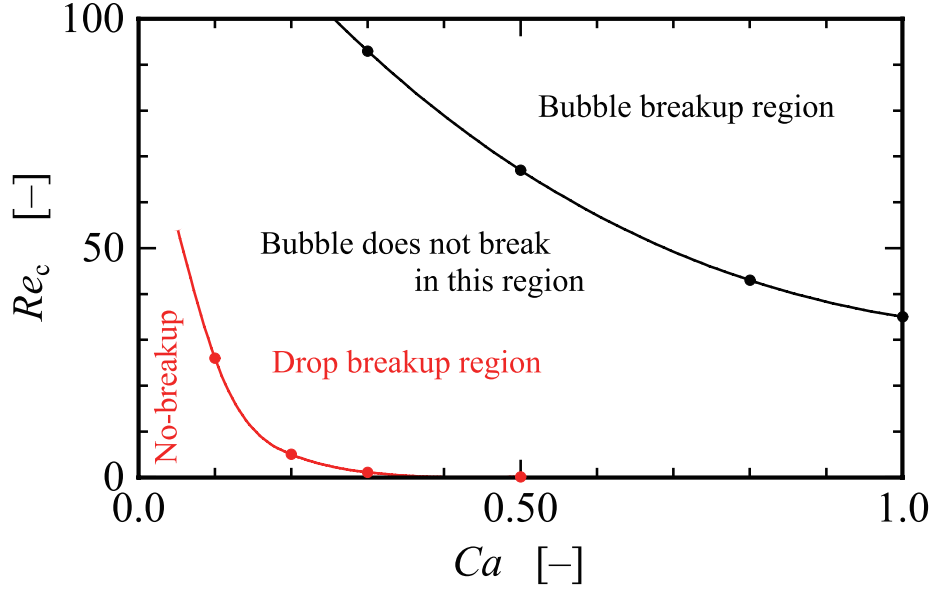


Figure 12: A plot of the critical Reynolds number versus Capillary number for the data listed in Table 4. $\lambda = 1.2 \times 10^{-3}$, $\eta < 1.0 \times 10^{-3}$, $0.3 < Ca < 1$, and the initial/boundary conditions are given by (1). Given a new data point, (Ca, Re) , one can reliably predict whether the given (Ca, Re) pair will result in shear induced bubble break-up or not. Note, for the “Drop delineation curve,” $\lambda = \eta = 1$.

533 numbers.

Table 4: Shear-induced bubble breakup for various flow conditions described in terms of column pairs of critical Reynolds numbers and corresponding Capillary numbers. ($\lambda = 1.2 \times 10^{-3}$, $\eta < 1.0 \times 10^{-3}$)

Capillary number Ca	0.3	0.5	0.8	1.0
Critical Reynolds number Re_c	93	67	43	35

534 5. Conclusions

535 The bubble deformation and breakup process in simple linear shear flow
 536 liquid was explored numerically using the CLSVOF computational method. In
 537 this study, the critical Reynolds number Re_c , at which bubble breakup first

538 occurs, was determined for several flow conditions, and the differences between
539 bubble deformation and breakup were compared with the well-known analogous
540 process of drop deformation and breakup.

541 Numerical results revealed significant differences between bubble deforma-
542 tion and breakup and the corresponding drop dynamics. For case of bubble,
543 it was discovered that much stronger shear flows are necessary to induce in-
544 terface breakup compared with a drop immersed in a similar flow field. That
545 is, a much larger Reynolds number flow is required in order to induce bubble
546 breakup. The behavior of bubble breakup was very similar through the Ca
547 number range considered in our computations: the bubble underwent a simi-
548 lar breakup mechanism in which rupture occurred at a thread-bridge part that
549 followed a doglegged shape formation stage. In bubble deformation without
550 breakup, near Re_c , the bubble did not maintain a stable deformed shape, in
551 contrast to drop deformation near the critical Reynolds number. The bubble
552 exhibited pronounced underdamped behavior: the bubble oscillated between
553 elongating and shrinking motions for non-rupturing flow conditions.

554 We attribute the large differences in morphology for the bubble undergo-
555 ing breakup, compared with the drop, to the density and viscosity ratio. The
556 density and viscosity ratio remarkably impacts on bubble/drop deformation
557 and breakup. The bubble deformation and breakup is subject to a synergistic
558 coupling of the density and viscosity ratio, and whose effect will be examined
559 separately in future work.

560 **References**

- 561 [1] Amani, A., Balcázar, N., Castro, J., Oliva, A., 2019. Nu-
562 matical study of droplet deformation in shear flow using a con-
563 servative level-set method. Chemical Engineering Science 207,
564 153–171. URL: <http://www.sciencedirect.com/science/article/pii/S0009250919305123>, doi:<https://doi.org/10.1016/j.ces.2019.06.014>.

- 567 [2] Bazhlekov, I.B., Anderson, P.D., Meijer, H.E., 2006. Numerical investi-
568 tigation of the effect of insoluble surfactants on drop deformation and
569 breakup in simple shear flow. *Journal of Colloid and Interface Science* 298,
570 369 – 394. URL: <http://www.sciencedirect.com/science/article/pii/S0021979705012658>, doi:<http://dx.doi.org/10.1016/j.jcis.2005.12.017>.
- 573 [3] Bento, D., Rodrigues, R.O., Faustino, V., Pinho, D., Fernandes, C.S.,
574 Pereira, A.I., Garcia, V., Miranda, J.M., Lima, R., 2018. Deforma-
575 tion of red blood cells, air bubbles, and droplets in microfluidic de-
576 vices: Flow visualizations and measurements. *Micromachines* 9. URL:
577 <https://www.mdpi.com/2072-666X/9/4/151>, doi:10.3390/mi9040151.
- 578 [4] Chu, P., Finch, J., Bournival, G., Ata, S., Hamlett, C., Pugh, R.J.,
579 2019. A review of bubble break-up. *Advances in Colloid and In-
580 terface Science* 270, 108–122. URL: <https://www.sciencedirect.com/science/article/pii/S0001868619300211>, doi:<https://doi.org/10.1016/j.cis.2019.05.010>.
- 583 [5] Cristini, V., Bławzdziewicz, J., Loewenberg, M., 2001. An adap-
584 tive mesh algorithm for evolving surfaces: simulations of drop breakup
585 and coalescence. *Journal of Computational Physics* 168, 445 –
586 463. URL: <http://www.sciencedirect.com/science/article/pii/S0021999101967130>, doi:<http://dx.doi.org/10.1006/jcph.2001.6713>.
- 588 [6] Cristini, V., Guido, S., Alfani, A., Bławzdziewicz, J., Loewenberg, M.,
589 2003. Drop breakup and fragment size distribution in shear flow. *Journal*
590 *of Rheology* 47, 1283–1298. URL: <http://scitation.aip.org/content/sor/journal/jor2/47/5/10.1122/1.1603240>, doi:<http://dx.doi.org/10.1122/1.1603240>.
- 593 [7] Croce, R., Griebel, M., Schweitzer, M.A., 2010. Numerical simulation of
594 bubble and droplet deformation by a level set approach with surface tension
595 in three dimensions. *International Journal for Numerical Methods in Fluids*

- 596 62, 963–993. URL: <http://dx.doi.org/10.1002/fld.2051>, doi:10.1002/fld.2051.
- 597
- 598 [8] Drenckhan, W., Saint-Jalmes, A., 2015. The science of foaming. Advances in Colloid and Interface Science 222, 228–259. URL: <https://www.sciencedirect.com/science/article/pii/S0001868615000603>, doi:<https://doi.org/10.1016/j.cis.2015.04.001>. reinhard Miller, Honorary Issue.
- 602
- 603 [9] Ervin, E., Tryggvason, G., 1997. The rise of bubbles in a vertical shear flow. Journal of Fluids Engineering 119(2), 443–449.
- 604
- 605 [10] Hernandez, F.H., Rangel, R.H., 2017. Breakup of drops in simple shear flows with high-confinement geometry. Computers & Fluids 146, 23 – 41. URL: <https://www.sciencedirect.com/science/article/pii/S0045793017300038>, doi:<https://doi.org/10.1016/j.compfluid.2017.01.001>.
- 606
- 607
- 608
- 609
- 610 [11] Hirt, C., Nichols, B., 1981. Volume of fluid (vof) method for the dynamics of free boundaries. Journal of Computational Physics 39, 201 – 225. URL: <https://www.sciencedirect.com/science/article/pii/0021999181901455>, doi:[http://dx.doi.org/10.1016/0021-9991\(81\)90145-5](http://dx.doi.org/10.1016/0021-9991(81)90145-5).
- 611
- 612
- 613
- 614
- 615 [12] Inamuro, T., 2006. Lattice boltzmann methods for viscous fluid flows and for two-phase fluid flows. Fluid Dynamics Research 38, 641. URL: <http://stacks.iop.org/1873-7005/38/i=9/a=A04>.
- 616
- 617
- 618 [13] Inamuro, T., Tomita, R., Ogino, F., 2003. Lattice boltzmann simulations of drop deformation and breakup in simple shear flows. International Journal of Modern Physics B 17, 21–26. URL: <http://www.worldscientific.com/doi/abs/10.1142/S0217979203017035>, doi:10.1142/S0217979203017035.
- 619
- 620
- 621
- 622

- 623 [14] Ioannou, N., Liu, H., Zhang, Y., 2016. Droplet dynamics
624 in confinement. Journal of Computational Science 17, 463 –
625 474. URL: <http://www.sciencedirect.com/science/article/pii/S1877750316300308>, doi:<https://doi.org/10.1016/j.jocs.2016.03.009>. discrete Simulation of Fluid Dynamics 2015.
- 626 [15] Janssen, P., Anderson, P., 2008. A boundary-integral model for
627 drop deformation between two parallel plates with non-unit viscosity
628 ratio drops. Journal of Computational Physics 227, 8807–
629 8819. URL: <http://www.sciencedirect.com/science/article/pii/S002199910800346X>, doi:<http://dx.doi.org/10.1016/j.jcp.2008.06.027>.
- 630 [16] Janssen, P.J.A., Anderson, P.D., 2007. Boundary-integral method
631 for drop deformation between parallel plates. Physics of Fluids
632 19. URL: <http://scitation.aip.org/content/aip/journal/pof2/19/4/10.1063/1.2715621>, doi:<http://dx.doi.org/10.1063/1.2715621>.
- 633 [17] Kang, M., Fedkiw, R.P., Liu, X.D., 2000. A boundary condition capturing
634 method for multiphase incompressible flow. Journal of scientific computing
635 15, 323–360.
- 636 [18] Khismatullin, D.B., Renardy, Y., Cristini, V., 2003. Inertia-induced
637 breakup of highly viscous drops subjected to simple shear. Physics of Fluids
638 15, 1351–1354. doi:<http://dx.doi.org/10.1063/1.1564825>.
- 639 [19] Komrakova, A., Shardt, O., Eskin, D., Derksen, J., 2014. Lattice
640 boltzmann simulations of drop deformation and breakup in shear flow.
641 International Journal of Multiphase Flow 59, 24 – 43. URL: <http://www.sciencedirect.com/science/article/pii/S0301932213001547>,
642 doi:<http://dx.doi.org/10.1016/j.ijmultiphaseflow.2013.10.009>.
- 643 [20] Komrakova, A., Shardt, O., Eskin, D., Derksen, J., 2015. Ef-
644 fects of dispersed phase viscosity on drop deformation and breakup
645

- 651 in inertial shear flow. Chemical Engineering Science 126, 150 –
652 159. URL: <http://www.sciencedirect.com/science/article/pii/S000925091400726X>, doi:<http://dx.doi.org/10.1016/j.ces.2014.12.012>.
- 653
- 654
- 655 [21] Legendre, D., Magnaudet, J., 1998. The lift force on a spherical bubble in
656 a viscous linear shear flow. Journal of Fluid Mechanics 368, 81–126.
- 657 [22] Li, J., Renardy, Y., Renardy, M., 2000. Numerical simulation of
658 breakup of a viscous drop in simple shear flow through a volume-of-fluid
659 method. Physics of Fluids 12, 269–282. URL: <http://scitation.aip.org/content/aip/journal/pof2/12/2/10.1063/1.870305>, doi:<http://dx.doi.org/10.1063/1.870305>.
- 660
- 661
- 662 [23] Müller-Fischer, N., Tobler, P., Dressler, M., Fischer, P., Windhab, E.J.,
663 2008. Single bubble deformation and breakup in simple shear flow. Experi-
664 ments in fluids 45, 917–926.
- 665 [24] Ohta, M., Kikuchi, D., Yoshida, Y., Sussman, M., 2011. Robust numeri-
666 cal analysis of the dynamic bubble formation process in a viscous liquid.
667 International Journal of Multiphase Flow 37, 1059–1071.
- 668 [25] Rallison, J.M., 1984. The deformation of small viscous drops
669 and bubbles in shear flows. Annual Review of Fluid Mechan-
670 ics 16, 45–66. URL: <http://dx.doi.org/10.1146/annurev.fl.16.010184.000401>,
671 doi:[10.1146/annurev.fl.16.010184.000401](http://dx.doi.org/10.1146/annurev.fl.16.010184.000401),
672 arXiv:<http://dx.doi.org/10.1146/annurev.fl.16.010184.000401>.
- 673 [26] Renardy, Y., 2006. Numerical simulation of a drop undergoing large am-
674 plitude oscillatory shear. Rheologica acta 45, 223–227.
- 675 [27] Renardy, Y., 2007. The effects of confinement and inertia on the production
676 of droplets. Rheologica Acta 46, 521–529. URL: <http://dx.doi.org/10.1007/s00397-006-0150-y>, doi:[10.1007/s00397-006-0150-y](http://dx.doi.org/10.1007/s00397-006-0150-y).
- 677

- 678 [28] Renardy, Y., 2008. Effect of startup conditions on drop breakup
679 under shear with inertia. International Journal of Multiphase Flow
680 34, 1185 – 1189. URL: <http://www.sciencedirect.com/science/article/pii/S030193220800089X>, doi:<http://dx.doi.org/10.1016/j.ijmultiphaseflow.2008.04.004>.
- 683 [29] Renardy, Y., Cristini, V., 2001a. Effect of inertia on drop breakup under
684 shear. Physics of Fluids 13, 7–13. URL: <http://scitation.aip.org/content/aip/journal/pof2/13/1/10.1063/1.1331321>, doi:<http://dx.doi.org/10.1063/1.1331321>.
- 687 [30] Renardy, Y., Cristini, V., Li, J., 2002. Drop fragment distributions un-
688 der shear with inertia. International Journal of Multiphase Flow 28, 1125
689 – 1147. URL: <http://www.sciencedirect.com/science/article/pii/S0301932202000228>, doi:[http://dx.doi.org/10.1016/S0301-9322\(02\)00022-8](http://dx.doi.org/10.1016/S0301-9322(02)00022-8).
- 692 [31] Renardy, Y.Y., Cristini, V., 2001b. Scalings for fragments produced
693 from drop breakup in shear flow with inertia. Physics of Fluids 13,
694 2161–2164. URL: <https://doi.org/10.1063/1.1384469>, doi:[10.1063/1.1384469](https://doi.org/10.1063/1.1384469), arXiv:<https://doi.org/10.1063/1.1384469>.
- 696 [32] Rust, A., Manga, M., 2002. Bubble shapes and orientations in low re-
697 simple shear flow. Journal of Colloid and Interface Science 249, 476–
698 480. URL: <https://www.sciencedirect.com/science/article/pii/S0021979702982925>, doi:<https://doi.org/10.1006/jcis.2002.8292>.
- 700 [33] Stone, H.A., 1994. Dynamics of drop deformation and breakup
701 in viscous fluids. Annual Review of Fluid Mechanics 26,
702 65–102. URL: <http://dx.doi.org/10.1146/annurev.fl.26.010194.000433>,
703 doi:[10.1146/annurev.fl.26.010194.000433](https://doi.org/10.1146/annurev.fl.26.010194.000433),
704 arXiv:<http://dx.doi.org/10.1146/annurev.fl.26.010194.000433>.
- 705 [34] Sussman, M., 2003. A second order coupled level set and volume-
706 of-fluid method for computing growth and collapse of vapor bub-

- bles. Journal of Computational Physics 187, 110–136. URL: <https://www.sciencedirect.com/science/article/pii/S0021999103000871>, doi:[https://doi.org/10.1016/S0021-9991\(03\)00087-1](https://doi.org/10.1016/S0021-9991(03)00087-1).
- [35] Sussman, M., Almgren, A.S., Bell, J.B., Colella, P., Howell, L.H., Welcome, M.L., 1999. An adaptive level set approach for incompressible two-phase flows. Journal of Computational Physics 148, 81 – 124. URL: <http://www.sciencedirect.com/science/article/pii/S002199919896106X>, doi:<https://doi.org/10.1006/jcph.1998.6106>.
- [36] Sussman, M., Puckett, E.G., 2000. A coupled level set and volume-of-fluid method for computing 3d and axisymmetric incompressible two-phase flows. Journal of Computational Physics 162, 301–337. URL: <http://www.sciencedirect.com/science/article/pii/S0021999100965379>, doi:<http://dx.doi.org/10.1006/jcph.2000.6537>.
- [37] Sussman, M., Smereka, P., Osher, S., 1994. A level set approach for computing solutions to incompressible two-phase flow. Journal of Computational Physics 114, 146 – 159. URL: <http://www.sciencedirect.com/science/article/pii/S0021999184711557>, doi:<http://dx.doi.org/10.1006/jcph.1994.1155>.
- [38] Sussman, M., Smith, K., Hussaini, M., Ohta, M., Zhi-Wei, R., 2007. A sharp interface method for incompressible two-phase flows. Journal of Computational Physics 221, 469–505. URL: <https://www.sciencedirect.com/science/article/pii/S0021999106002981>, doi:<https://doi.org/10.1016/j.jcp.2006.06.020>.
- [39] Tanguy, S., Ménard, T., Berlemont, A., 2007. A level set method for vaporizing two-phase flows. Journal of Computational Physics 221, 837–853.
- [40] Taylor, G.I., 1932. The viscosity of a fluid containing small drops of another fluid. Proceedings of the Royal Society of London A: Mathematical, Physical and Engineering Sciences 138, 41–48. doi:[10.1098/rspa.1932.0169](https://doi.org/10.1098/rspa.1932.0169).

- 736 [41] Taylor, G.I., 1934. The formation of emulsions in definable fields of flow.
737 Proceedings of the Royal Society of London A: Mathematical, Physical and
738 Engineering Sciences 146, 501–523. doi:10.1098/rspa.1934.0169.
- 739 [42] Unverdi, S.O., Tryggvason, G., 1992. A front-tracking method
740 for viscous, incompressible, multi-fluid flows. Journal of Computational
741 Physics 100, 25 – 37. URL: <http://www.sciencedirect.com/science/article/pii/002199919290307K>, doi:[http://dx.doi.org/10.1016/0021-9991\(92\)90307-K](http://dx.doi.org/10.1016/0021-9991(92)90307-K).
- 744 [43] Wang, Z., Shi, D., Zhang, A., 2015. Three-dimensional lattice boltzmann simulation of bubble behavior in a flap-induced shear flow. Computers & Fluids 123, 44 – 53. URL: <http://www.sciencedirect.com/science/article/pii/S0045793015003199>, doi:<https://doi.org/10.1016/j.compfluid.2015.09.007>.
- 749 [44] Wei, Y.K., Qian, Y., Xu, H., 2012. Lattice boltzmann simulations
750 of single bubble deformation and breakup in a shear flow. The Journal
751 of Computational Multiphase Flows 4, 111–117. URL: <https://doi.org/10.1260/1757-482X.4.1.111>, doi:10.1260/1757-482X.4.1.
753 111, arXiv:<https://doi.org/10.1260/1757-482X.4.1.111>.
- 754 [45] Zhang, J., Miksis, M.J., Bankoff, S.G., 2006. Nonlinear dynamics of
755 a two-dimensional viscous drop under shear flow. Physics of Fluids
756 18. URL: <http://scitation.aip.org/content/aip/journal/pof2/18/7/10.1063/1.2222336>, doi:<http://dx.doi.org/10.1063/1.2222336>.
- 758 [46] Zhang, J., Ni, M.J., Magnaudet, J., 2021a. Three-dimensional dynamics
759 of a pair of deformable bubbles rising initially in line. part 1. moderately
760 inertial regimes. Journal of Fluid Mechanics 920, A16.
- 761 [47] Zhang, J., Ni, M.J., Magnaudet, J., 2022. Three-dimensional dynamics of
762 a pair of deformable bubbles rising initially in line. part 2. highly inertial
763 regimes. Journal of Fluid Mechanics 943, A10.

- 764 [48] Zhang, J., Shu, S., Guan, X., Yang, N., 2021b. Regime map-
765 ping of multiple breakup of droplets in shear flow by phase-field
766 lattice boltzmann simulation. Chemical Engineering Science 240,
767 116673. URL: <https://www.sciencedirect.com/science/article/pii/S0009250921002384>, doi:<https://doi.org/10.1016/j.ces.2021.116673>.
768
769